Electronic Supplementary Material (ESI) for Energy & Environmental Science.

Supporting Information for

Solar-driven electrochemical synthesis of ammonia using nitrate with 11% solar-to-fuel efficiency at ambient conditions

Nishithan C. Kani[1], Joseph A. Gauthier[2,3,4*], Aditya Prajapati[1], Jane Edgington[5], Isha Bordawekar[6], Windom Shields[7], Mitchell Shields[7], Linsey C. Seitz[5], Aayush R. Singh[8*], and Meenesh R. Singh[1*]

[1]Department of Chemical Engineering, University of Illinois at Chicago, Chicago, IL 60607

[2]Chemical Sciences Division, Lawrence Berkeley National Laboratory, Berkeley, CA 94720

[3]Department of Chemical and Biomolecular Engineering, University of California, Berkeley, CA 94720

[4]Department of Chemical Engineering, Texas Tech University, Lubbock, TX 79409

[5]Department of Chemical and Biological Engineering, Northwestern University, Evanston, IL 60208.

[6]Warren Township High School, Gurnee, IL 60031

[7]Worldwide Liquid Sunshine LLC, Maple Plain, MN 55359

[8]Dow Inc., Midland, MI 48686

Corresponding Authors:

Prof. Meenesh R. Singh, Tel: (312) 413-7673, Email: mrsingh@uic.edu
Dr. Joseph A. Gauthier, Email: joe.gauthier@ttu.edu
Dr. Aayush R. Singh, Email: ARSingh@dow.com

Keywords: Solar-to-Fuel Efficiency, Electrocatalysis, Electrochemical Nitrate Reduction, Electrochemical Ammonia Synthesis

S1. Literature Summary

Sl. No.	Catalyst	Electrolyte	Maximum Faradaic Efficiency (%)	Maximum NH_3 Current Density (mA/cm^2)	Reference
1	Ti	1M KOH	82 (-1 V vs RHE)	-22 (-1 V vs RHE)	[1]
2	$Cu_{50}Ni_{50}$/PTFE/CuFoam	1M KOH	~100 (-0.15 V vs RHE)	-90 (-0.1 V vs RHE)	[2]
3	Cu/Cu_2O Nanowires	0.5 M Na_2SO_4	95.80 (-0.85 V vs RHE)	-52.5 (-0.85 V vs RHE)	[3]
4	Cu-PTCDA/Carbon cloth	0.1 M PBS	85.90 (-0.4 V vs RHE)	-11.04 (-0.6 V vs RHE)	[4]
5	Fe SAC	0.1 M K_2SO_4	75 (-0.66 V vs RHE)	-100 (-0.85 V vs RHE)	[5]
6	Co Nanoarrays	1 M KOH/0.5 M K_2SO_4	96 (-0.24 V vs RHE)	-2200 (-0.24 V vs RHE)	[6]
7	OD-Co	1 M KOH	92.37 ± 6.7 (-0.8 V vs RHE)	-0.288 565.26 (-0.8 V vs RHE)	This work

Table S1: Literature comparison of the NH_3 current densities and NH_3 Faradaic efficiencies from the electrochemical reduction of nitrates.

Sl. No.	Catalyst	ECSA(cm^2)	Normalized Current Density (mA/cm^2-ECSA)	Reference
1	$Cu_{50}Ni_{50}$/PTFE/CuFoam	61.25	- 0.288	[2]
2	Cu/Cu_2O Nanowires	25	-6.3	[3]
3	Fe SAC	52.75	-3.739	[5]
4	Co Nanoarrays	80.267	-6.8521	[6]
5	OD-Co	11.998	-13.319	This Work

Table S2: Literature comparison of the NH_3 current densities normalized to ECSA.

S2. Materials

Chemicals

Sl. No.	Chemical	Purity/Name	Manufacturer
1	Potassium Nitrate	>99%	Sigma Aldrich
2	Potassium Hydroxide	>85%	Sigma Aldrich
3	Fuming Nitric Acid	>90%	Sigma Aldrich
4	Alkaline Hypochlorite	>99%	Sigma Aldrich
5	Phenol Nitroprusside	>99%	Sigma Aldrich
6	Cobalt Nitrate	>98%	Sigma Aldrich
7	Potassium phosphate monobasic	>99%	Sigma Aldrich
8	Potassium phosphate dibasic	>98%	Sigma Aldrich
9	3D Print Resin	FLGPCL04	Formlabs

Membranes/Substrates

Sl. No.	Substance	Manufacturer
1	Excellion Membrane	Fuel cell store
2	Carbon Paper	Fuel cell store
3	Nafion	Fuel cell store
4	PTFE	Sigma Aldrich
5	Carbon Planchet	Ted Pella
6	Cobalt	ACI Alloys

Instruments

Sl. No.	Instrument	Name/Manufacturer
1	Potentiostat	SP-300/Biologic
2	Visible Spectrometer	Genysys 30/Thermo Fischer
3	X-Ray Diffractometer	D8 ADVANCE/Bruker
4	X-Ray Photoelectron Spectrometer	Axis-165/Kratos Analytical
5	Solar Simulator	LCS-100/Ariel Instruments
6	Solar Cell	Spectrolabs
7	IR Spectrometer	Invenio S/Bruker
8	3D Printer	Form 3/Formlabs

S3. Reaction Mechanism – DFT Calculations

Following the approach of Goldsmith and coworkers[7,8], we consider the following mechanism for electrochemical nitrate reduction:

$$HNO_3(aq) + (H^+ + e^-) + * \rightarrow H_2O(l) + NO_2* \quad \text{(i)}$$

$$NO_2^* + (H^+ + e^-) \rightarrow NO_2H^* \quad \text{(ii)}$$

$$NO_2H^* + (H^+ + e^-) \rightarrow NO^* + H_2O(l) \quad \text{(iii)}$$

$$NO^* + (H^+ + e^-) \rightarrow NOH^* \quad \text{(iv)}$$

$$NOH^* + (H^+ + e^-) \rightarrow N^* + H_2O(l) \quad \text{(v)}$$

$$N^* + (H^+ + e^-) \rightarrow NH^* \quad \text{(vi)}$$

$$NH^* + (H^+ + e^-) \rightarrow NH_2^* \quad \text{(vii)}$$

$$NH^* + (H^+ + e^-) \rightarrow NH_2^* \quad \text{(viii)}$$

$$NH_3^* \rightarrow NH_3(g) + * \quad \text{(ix)}$$

Binding energies were calculated relative to N_2, H_2, and O_2. To avoid DFT errors associated with ions and the triplet state of O_2, experimental formation energies were used to define the energies of gas phase H_2O, HNO_3, and NO_3^-. We note that our choice of reference means that Eq. (i) of our mechanism is equivalent to the reaction,

$$NO_3^-(aq) + 2H^+ + e^- + * \rightarrow H_2O(l) + NO_2^* \quad \text{(x)}$$

giving an overall reaction,

$$NO_3^-(aq) + 9H^+ + 8e^- \rightarrow NH_3(g) + 3H_2O(l) \quad \text{(xi)}$$

Binding energies were calculated as,

$$\Delta G_{rxn} = \Delta E_{DFT} + \Delta E_{ZPE} - T\Delta S_o - eU$$

with E_{DFT} being the total energy as calculated with DFT, E_{ZPE} the zero-point energy contribution to the free energy, T the temperature (in this case 300K), S_0 the entropy assuming adsorbates have only vibrational degrees of freedom (no rotation or translation), and $-eU$ the free energy contribution from the electron chemical potential.

S4. X-Ray Absorption Spectroscopy (XAS)

All EXAFS fits (**Figure S1**) were performed using a k-range of 3.00-12.25 and an R-range of 1-4. The best fit for the Co metal foil and Co metal thin film sample was generated using three Co-Co paths, and a total of 8 fitting parameters. The coordination number of each path for the Co metal and foil and Co metal thin film sample were fixed, enabling the determination of the S_0^2 value for both the Co metal foil and Co metal thin film sample. Due to the differences in measurement and sample geometry between the Co metal foil and Co metal thin film sample, the determined S_0^2 varied significantly. The S_0^2 calculated for the Co metal thin film sample was used and fixed for the OD Co thin film sample, allowing the determination of coordination number in the OD Co thin film. When fit with only the three Co-Co paths, a good fit was not able to be obtained for the OD Co thin film. An additional Co-O path was required, located at 2.145 Å, to obtain a good fit for the OD Co thin film sample. Goodness of fit statistics are provided in **Table S4**.

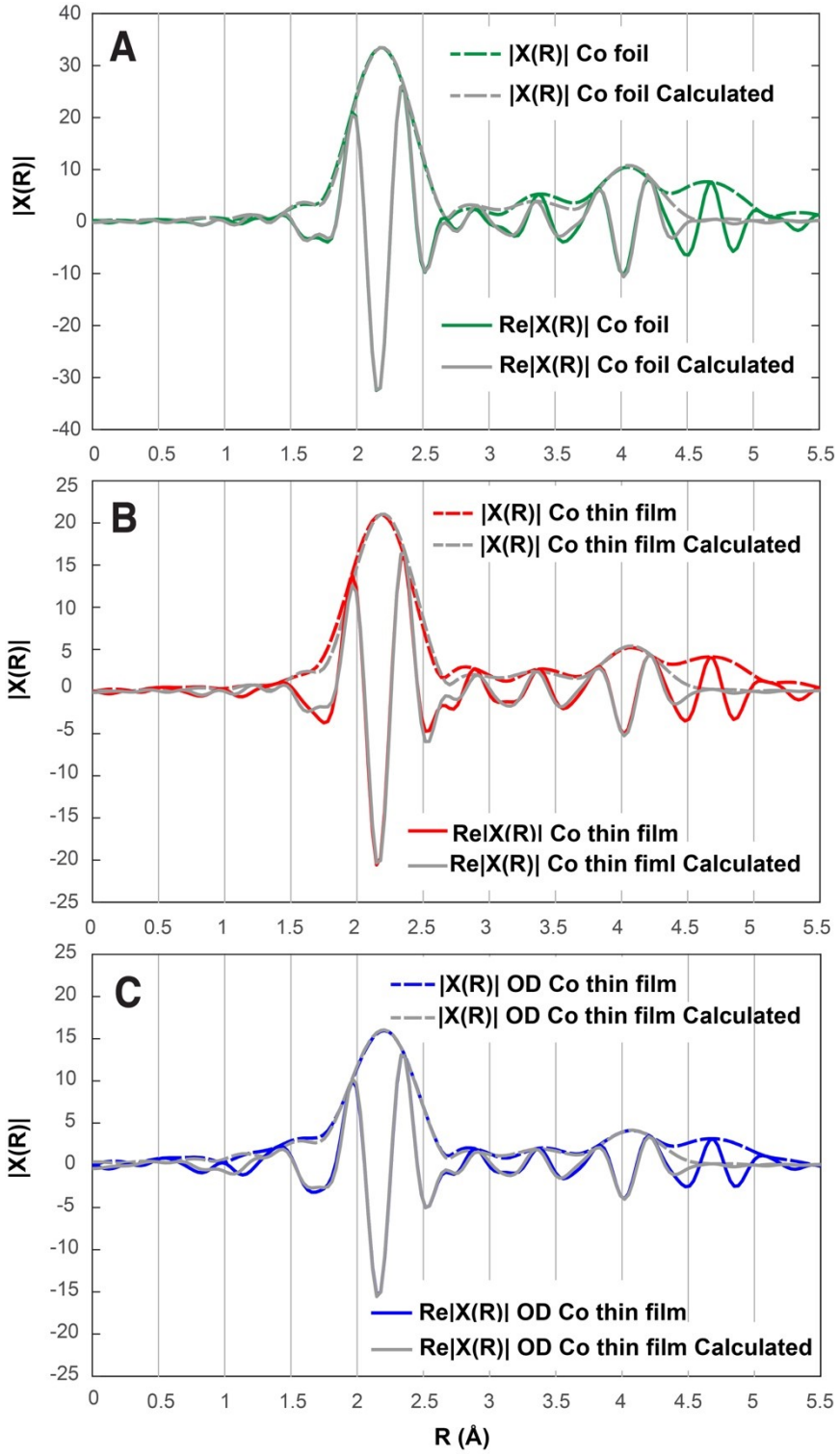

Figure S1: A) EXAFS spectra and calculated fit of the reference Co foil. B) EXAFS spectra and calculated fit of the pristine Co film atop a glassy carbon sheet substrate. C) EXAFS spectra and calculated fit of the OD-Co film atop a glassy carbon sheet substrate.

Sample	Path Name	N	S_0^2	σ^2	E_0	ΔR	R_{eff}	R
Co Foil Reference	[Co_mp-102] Co.1	12	0.781	0.0065	9.149	0.008	2.490	2.498
	[Co_mp-102] Co.2	6	0.781	0.0112	9.149	-0.021	3.521	3.500
	[Co_mp-102] Co.3	24	0.781	0.0096	9.149	0.056	4.312	4.368
		N	S_0^2	σ^2	E_0	ΔR	R_{eff}	R
Pristine Co Metal Film	[Co_mp-102] Co.1	12	0.57	0.0076	9.894	0.013	2.490	2.503
	[Co_mp-102] Co.2	6	0.57	0.0122	9.894	-0.016	3.521	3.505
	[Co_mp-102] Co.3	24	0.57	0.0127	9.894	0.066	4.312	4.379
		N	S_0^2	σ^2	E_0	ΔR	R_{eff}	R
OD Co Film	[Co_mp-102] Co.1	9.0	0.57	0.0073	9.724	0.009	2.490	2.498
	[Co_mp-102] Co.2	4.5	0.57	0.0118	9.724	-0.021	3.521	3.500
	[Co_mp-102] Co.3	18.1	0.57	0.0126	9.724	0.059	4.312	4.372
	[CoO_mp-19079] O.1	4.5	0.57	0.0286	9.724	-0.147	2.145	1.998

Table S3: EXAFS fitted parameters

Sample	Reduced chi-square	R-factor
Co foil	4307.0	0.0157
Pristine Co film	609.5	0.0191
OD Co film	368.2	0.0135

Table S4: EXAFS goodness of fit indicators

S5. Electrochemical Cell – ATR-SEIRAS studies

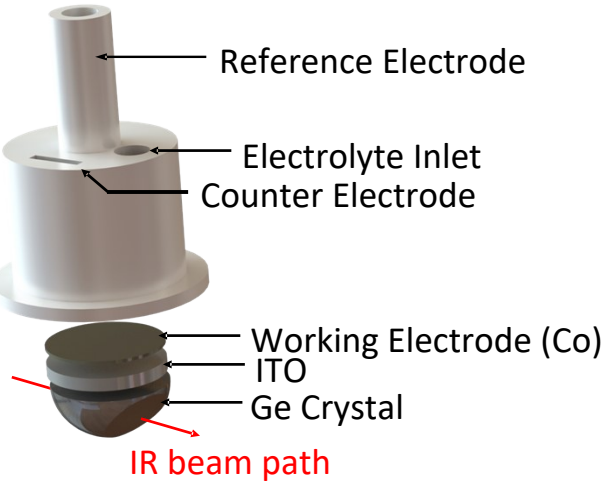

Figure S2: Experimental setup for ATR-SEIRAS studies

S6. Electrochemical Cell – H-cell configuration

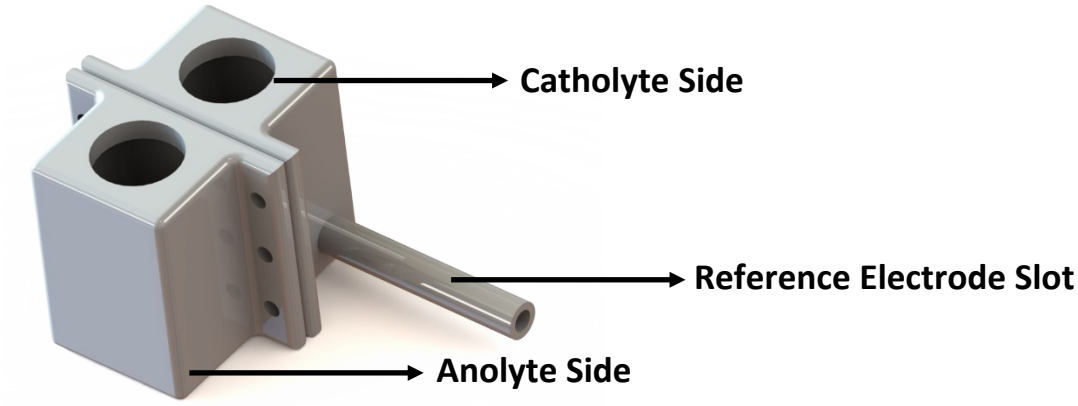

Figure S3: A 3D model of the electrochemical cell used for the experiments. CAD files are available upon request.

Figure S3 denotes the electrochemical cell model used for all the experiments. The electrochemical cell was designed in SolidWorks 2020 and 3D printed using Form3 3D printer (Formlabs). The anolyte and the catholyte sides were separated by using a quaternary ammonium anion exchange membrane (Excellion). The cobalt electrode was placed on the catholyte side, and the Platinum electrode was placed on the anolyte side. Ag/AgCl/KCl was inserted in the reference electrode slot. Both the anolyte and the catholyte chambers were tightly screwed and it was checked for leaks.

S7. NH_3 Quantification

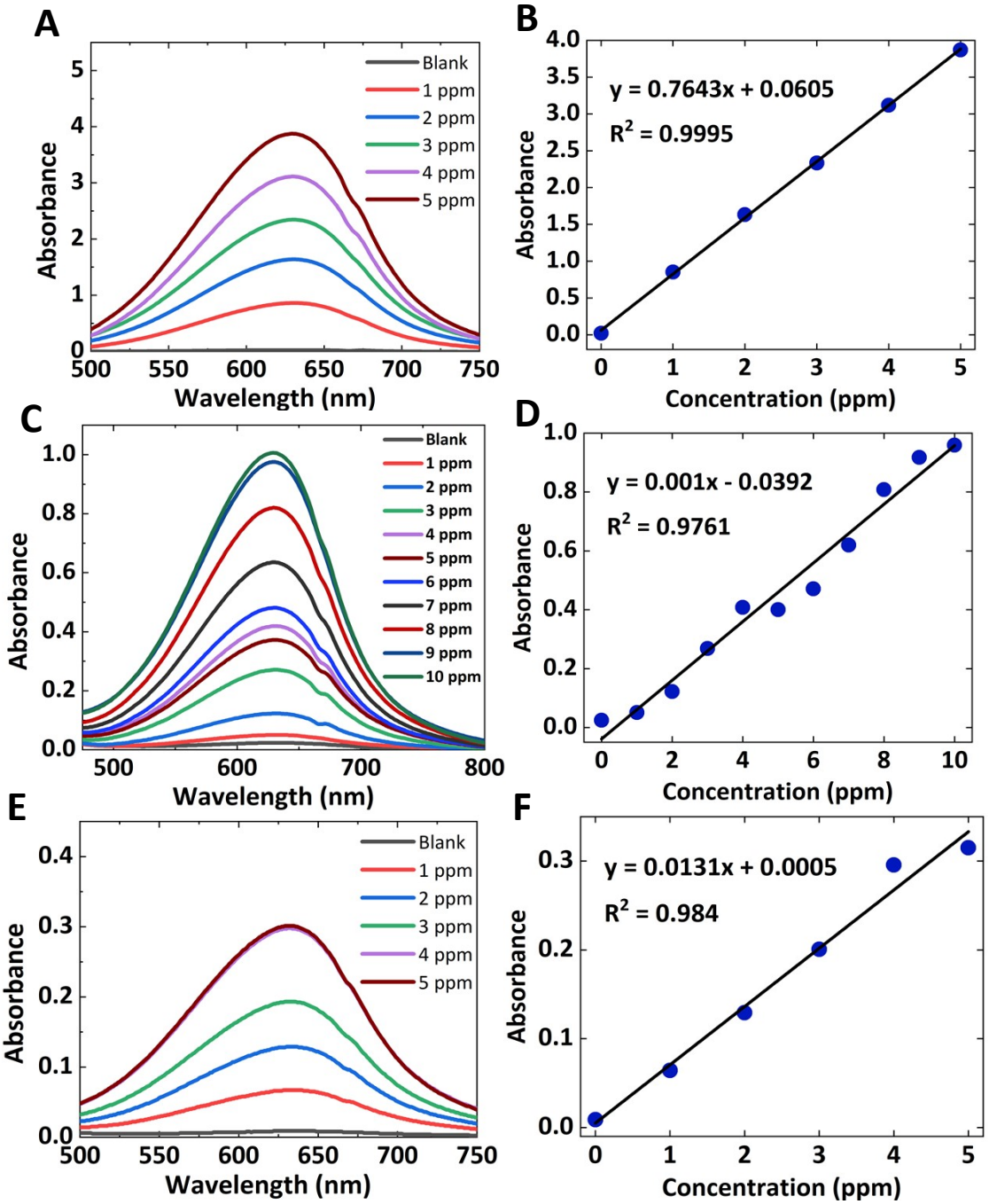

Figure S4: Calibration Graphs for Ammonia quantification. A) Absorbance spectra for standard solutions of ammonia at pH 7. B) Absorbance as a function of Concentrations of Ammonia (pH = 7) at 632 nm. C) Absorbance spectra for standard solutions of ammonia at pH 14. D) Absorbance as a function of Concentrations of Ammonia (pH = 14) at 632 nm. E) Absorbance spectra for standard solutions of ammonia at pH 1. F) Absorbance as a function of Concentrations of Ammonia (pH = 1) at 632 nm.

S8. Solar Cell Characterization

Figure S5 shows the characterization curves for the solar cell. j-V characteristics curve was obtained by doing a potential sweep at a rate of 10 mV/s between 0 and 3 V. Comparison was made between illumination using ambient light (**Figure S5A**) and AM 1.5 G (**Figure S5B**). Power was calculated by multiplying the absolute value of the current with the applied potential. **Table S5** indicates the parameters obtained from the solar cell characterization. The total area of the solar cell illuminated by using simulated AM 1.5 G sunlight was 16 cm^2. Open circuit potential (E_{oc}) is the potential at which the current is 0 and short circuit current (I_{sc}) is the current at which the potential is 0. Theoretical maximum power is the product between I_{sc} and E_{oc}. Maximum power (P_{max}) obtained from the solar cell is found from the power-voltage curve and the current corresponding to that is the maximum current (I_{max}) and the potential corresponding to that is the maximum potential (E_{max}). Fill Factor (FF) is the ratio between the maximum power obtained from the solar cell and the theoretical maximum power. The efficiency of the solar cell is defined as the ratio between the maximum power obtained from the solar cell and the power input to the solar cell (AM 1.5 G – 1 Sun is 100 mW/cm^2). The open-circuit current was measured as a function of time by using the potentiostat as a zero-resistance ammeter (**Figure S5E**).

Sl.No.	Parameter	Value
1	Area illuminated	16 cm^2
2	Open circuit potential (E_{oc})	2.50127 V
3	Short circuit current (I_{sc})	463.08 mA
4	Theoretical maximum power	1158.288 mW
5	Maximum potential (E_{max})	1.70664 V
6	Maximum current (I_{max})	438.998 mA
7	Maximum power (P_{max})	749.2115 mW
8	Power input (P_{in})	100 mW/cm^2
9	Fill Factor (FF)	0.6468
10	Efficiency (η)	46.83 %

Table S5: Solar Cell Characterization - Parameters

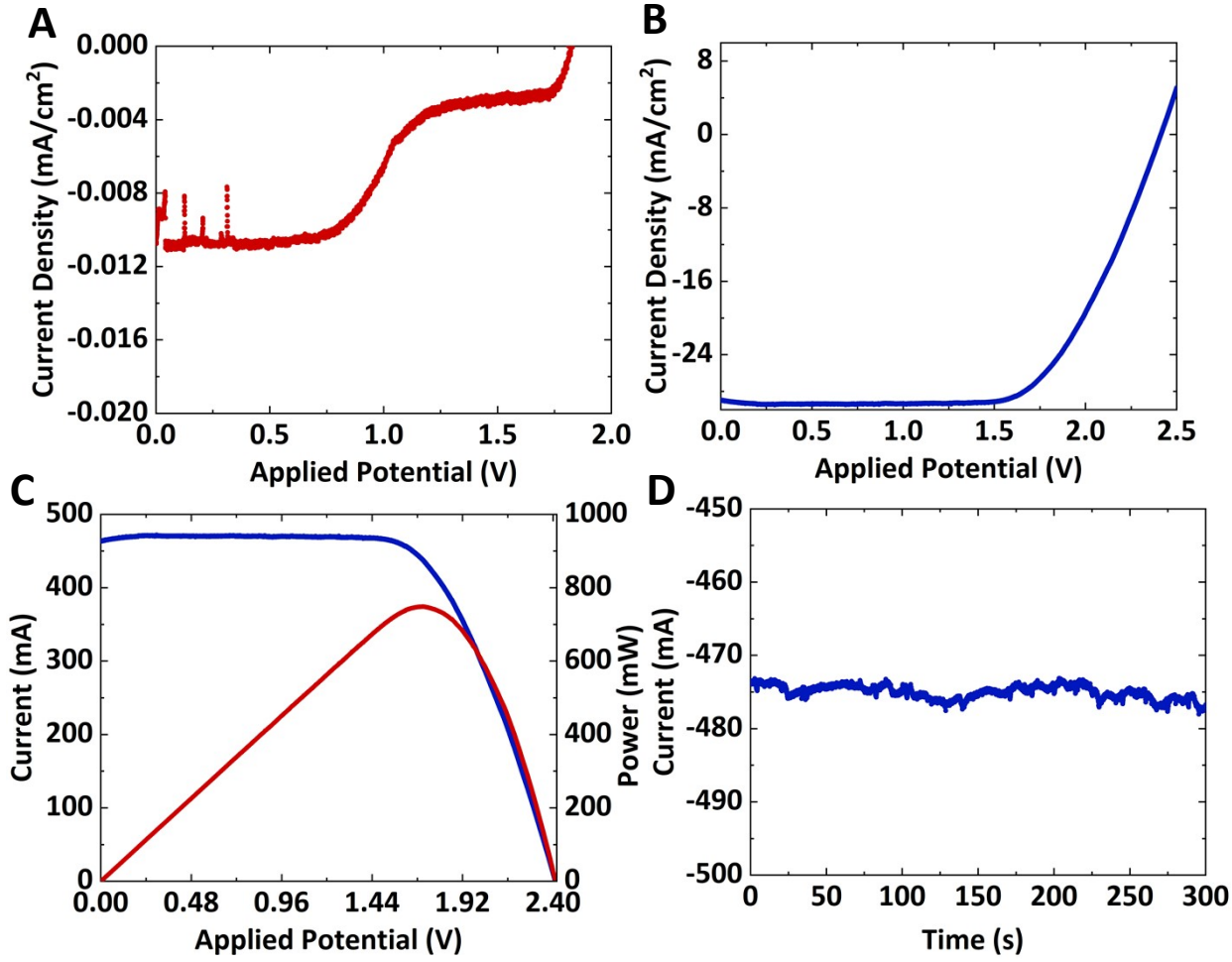

Figure S5: Solar Cell Characterization: A) j-V characteristics of the solar cell under ambient diffuse light illumination. B) j-V characteristics of the solar cell under AM 1.5 G illumination. C) Power-Current-Voltage curve (absolute values were plotted) for the solar cell under AM 1.5 G illumination. D) Open circuit current of the solar cell as a function of time.

S9. DFT Calculations – Linear Scaling Relations

Linear scaling relations were utilized to map the binding energy of every intermediate onto a single descriptor, in this case, the binding energy of atomic nitrogen. Four of the most important scaling relations are shown below in **Figure S6**. In our limiting potential model, the activity of a catalyst is approximated by the largest reaction free energy change at no applied bias between the steps listed in Eqs. i-ix (section S3). More active catalysts will have a smaller maximum free energy change, and therefore be higher on the activity volcano shown in Figure 1(a) of the main text. The limiting potential volcano with all reactions tested is shown in **Figure S7**. All other reactions tested are more favorable than the limiting reactions.

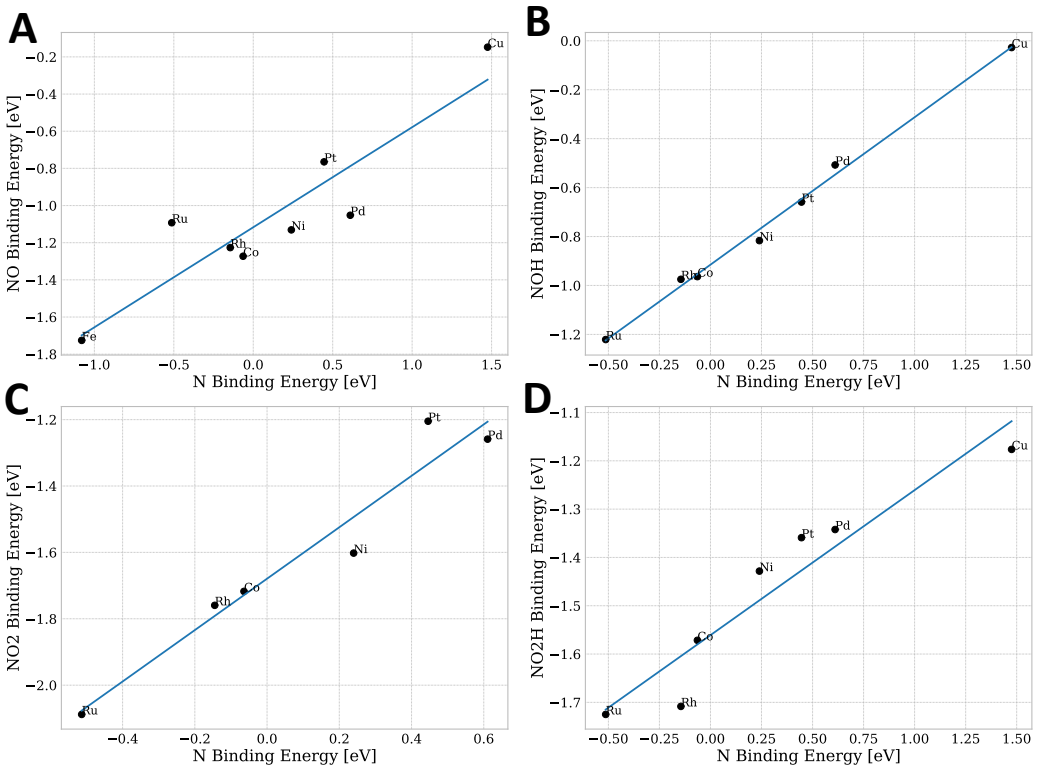

Figure S6: Scaling lines for mapping critical intermediates for electrochemical nitrate reduction onto the atomic nitrogen binding energy. A) NO. B) NOH. C) NO_2. D) NO_2H.

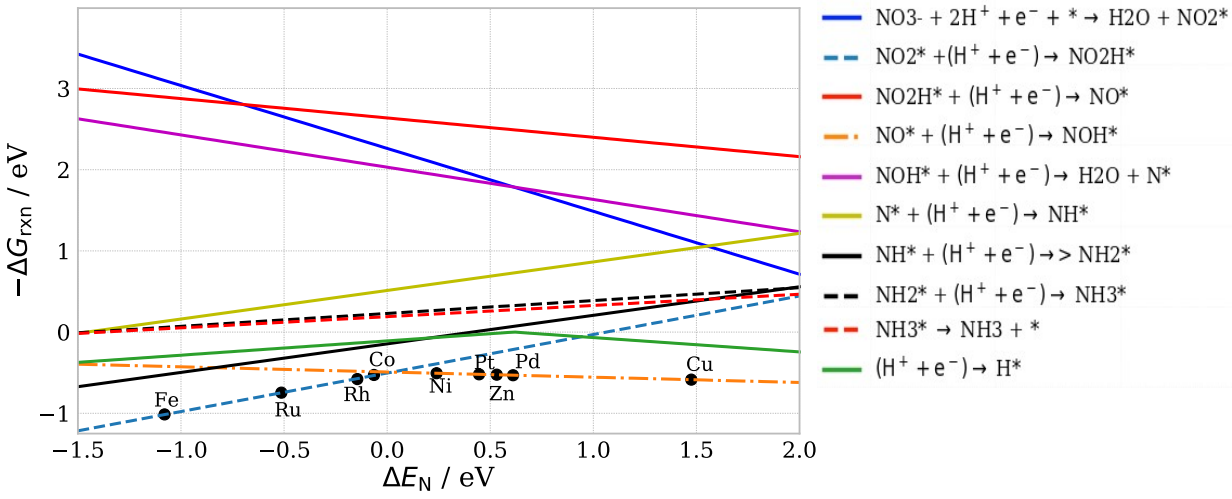

Figure S7: Activity volcano with all reactions tested shown.

S10. ECSA Calculations

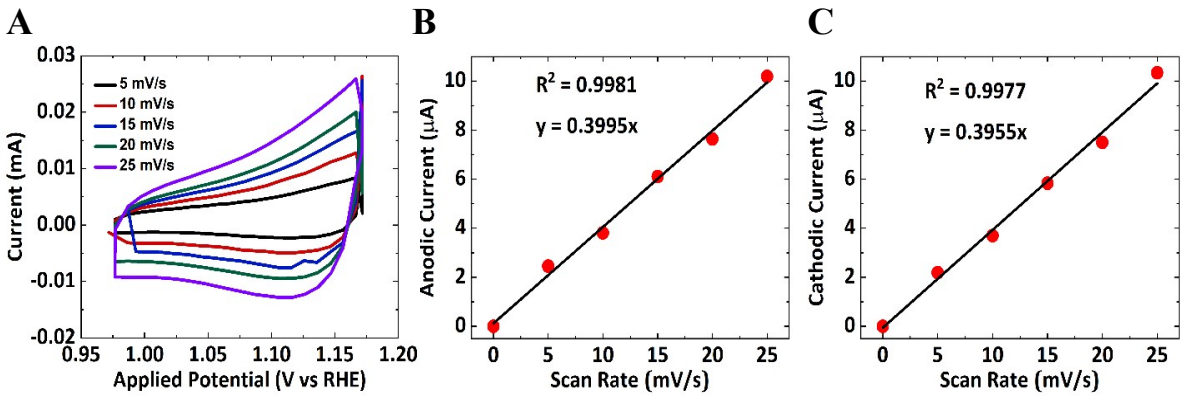

Figure S8: Double layer capacitance measurements to determine electrochemically active surface area (ECSA) of Cobalt in 0.1 M KOH: A) Cyclic Voltammograms in a non-Faradaic region window at different voltage scan rates. B) Anodic currents measured at 1.05 V vs RHE as a function of voltage scan rates. C) Cathodic currents measured at 1.05 V vs RHE as a function of voltage scan rates. (The absolute value of the currents is plotted)

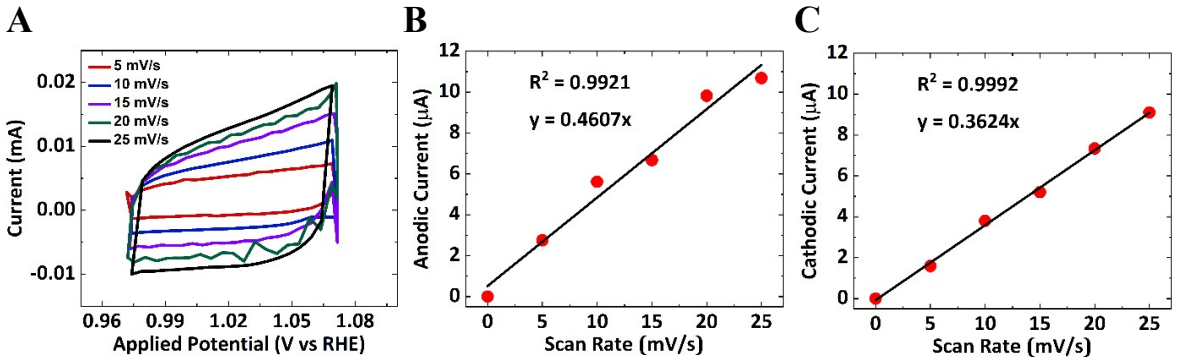

Figure S9: Double layer capacitance measurements to determine electrochemically active surface area (ECSA) of oxide-derived Cobalt in 0.1 M KOH: A) Cyclic Voltammograms in a non-Faradaic region window at different voltage scan rates. B) Anodic currents measured at 1 V vs RHE as a function of voltage scan rates. C) Cathodic currents measured at 1 V vs RHE as a function of voltage scan rates. (The absolute value of the currents is plotted)

Electrochemically active surface area is estimated as the ratio between double layer capacitance and specific capacitance (0.0375 mF/cm^2)[9,10]. The steps mentioned in the article by Risch et al.[11] were followed to minimize the errors. Double layer capacitance was estimated by performing cyclic voltammetry (CV) in the non-Faradaic region at different scan rates 5, 10, 15, 20, and 25 mV/s. The anodic and cathodic currents at 1.05 V vs RHE for Co and 1 V vs RHE for OD-Co were plotted as a function of the voltage scan rates. Linear regression was performed to determine the slope which is the double layer capacitance. An average value was taken between the double layer

capacitances measured from anodic and cathodic currents. **Figure S8** denotes the double layer capacitance measurements for Co and **Figure S9** denotes the double layer capacitance measurements for OD-Cobalt. For Co, the ECSA was estimated to be 10.6 cm^2 and for OD-Co the ECSA was estimated to be 10.975 cm^2.

S11. Surface Roughness Measurements

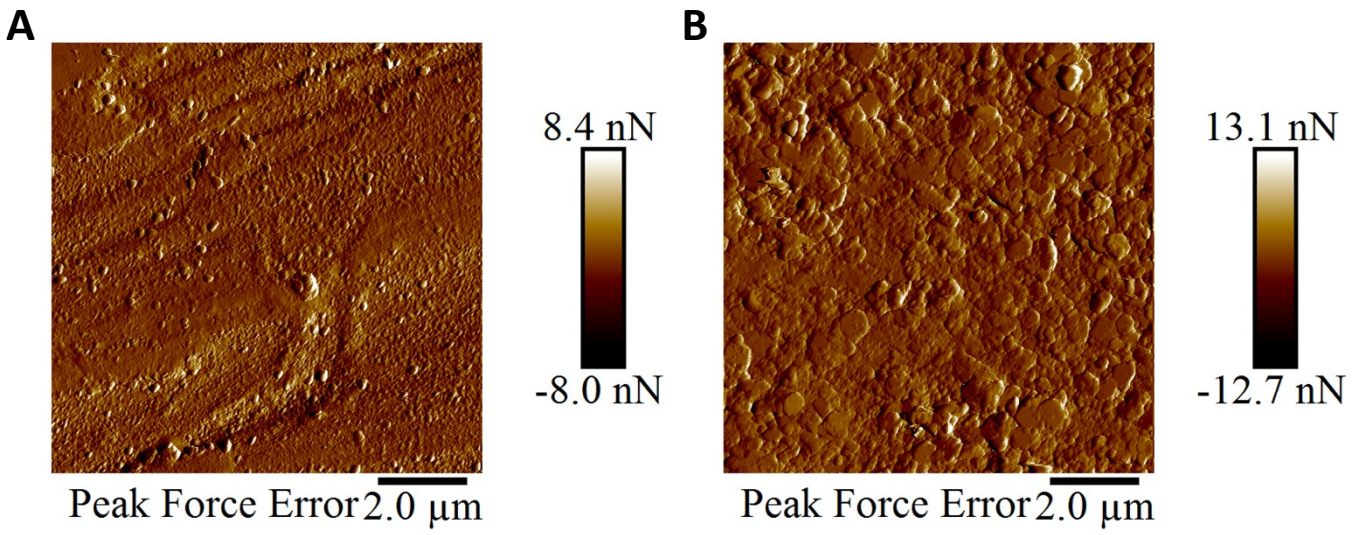

Figure S10: Atomic Force Microscopy Images of Cobalt (A) and Oxide-Derived Cobalt (B)

Atomic Force Microscope (AFM) images were acquired using a Bruker Dimension Icon Atomic Force Microscope in the Nanotechnology Core Facility (NCF) of UIC. AFM was performed for surface analysis to measure the maximum surface roughness, and the roughness factor. The roughness parameters were calculated and indicated in ***Table S6***. Based on the analysis we can conclude that the OD-Co surface is rougher than the Co surface which explains the improved performance of the electrochemical nitrate reduction on OD-Co.

Sl. No.	Catalyst	Maximum Surface Roughness (R max, nm)	Roughness Factor (RF) %
1	Co	615 nm	7.3
2	OD-Co	785 nm	20.4

Table S6: Surface Analysis using AFM

S12. FTIR Measurements

Two crucial parameters to determine the successful performance of ATR-SEIRAS experiments are the determination of the critical angle of incidence and the depth of penetration at an angle of incidence. The critical angle is the minimum angle at which the incident IR beam will not be internally reflected. This is the minimum angle required to ensure that the incident IR beam will reach the surface of the ATR crystal and the catalyst surface coating on it to generate the evanescent wave that helps in probing the catalyst surface. The critical angle can be calculated by:

$$\theta_c = \sin^{-1}(n_2 / n_1)$$

where θ_c is the critical angle, n_1 is the refractive index of the ATR crystal (Ge;4), and n_2 is the refractive index of the catalyst (Co; 2.81). The critical angle for this setup is 44.62°. Therefore, the experiments are conducted at an angle of incidence larger than 44.62°.

Depth of penetration is another parameter that indicates how far above the surface of the catalyst the detection of the species is possible. This depth is a function of the angle of incidence, the refractive index of the catalyst and the crystal, and the incident wavelength. It can be calculated as:

$$d_p = \frac{\lambda}{2\pi n_1 \sqrt{\sin^2\theta - \left(\frac{n_1}{n_2}\right)^2}}$$

where λ is the incident wavelength, and θ is the angle of incidence. From the above equation, the depth of penetration will be very large if θ is very close to θ_c. Since we are working in an aqueous environment with a highly concentrated electrolyte that absorbs IR readily, it is advisable to have a depth of penetration as low as possible so that only the surface above the catalyst is detected thereby avoiding signal loss due to the aqueous medium. An angle of incidence of 60° was chosen as Ge is a 60° face-angled crystal and gives a maximum signal at this angle while keeping a maximum depth of penetration to 4 μm as seen in **Figure S12**.

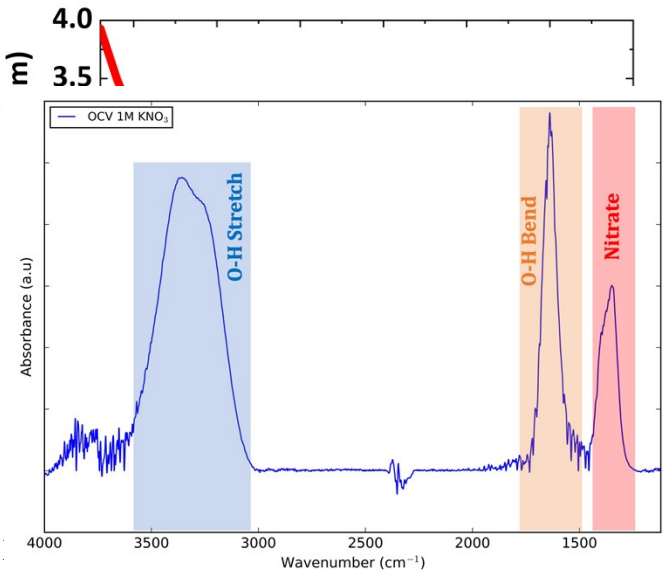

Figure S11: Depth of

Figure S12: FTIR spectrum of 1 M KNO_3 at an open-circuit voltage (OCV).

S13. Gas Chromatogram

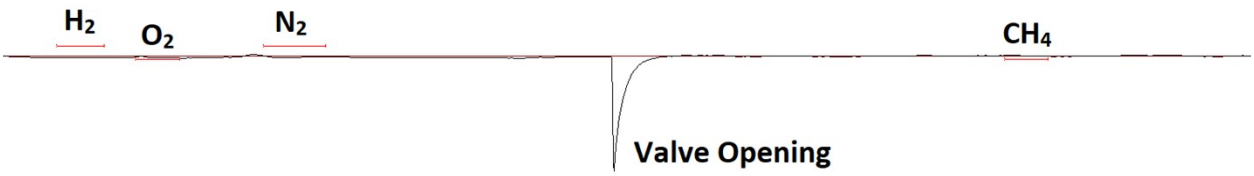

Figure S13: Gas Chromatogram from the TCD Channel indicating no observable peaks for H_2, and N_2.

S14. Tafel Slope

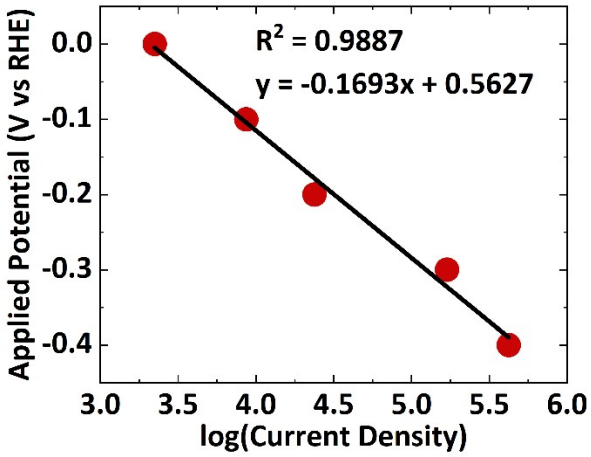

Figure S14: Tafel Slope Calculations.

Chronoamperometry was performed at different applied potentials of 0, -0.1, -0.2, -0.3, and -0.4 V vs RHE at pH = 14. The potentials less than -0.4 were considered. The current was measured at these potentials. Applied potential was plotted as a function of the logarithmic values of the current density. The slope was found which is the Tafel slope. The Tafel slope is estimated to be 169.3 mV/decade.

S15. Simulated Wastewater Reduction

Simulated wastewater was prepared with the following composition (3 mM Nitrates, Nitrites, Carbonates, Bicarbonates, Phosphates, Sulphates) and the pH was maintained at 8.5. NH_3 current density and NH_3 Faradaic efficiency were measured by varying the applied potentials. A maximum NH_3 Faradaic efficiency of ~ 12% and an NH_3 current density of ~ 1 mA/cm^2 were obtained.

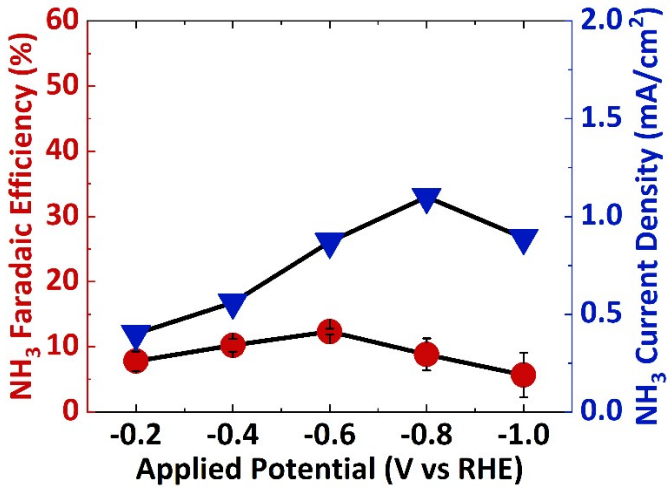

Figure S15: Effect of Applied Potential for the electrochemical reduction of simulated wastewater.

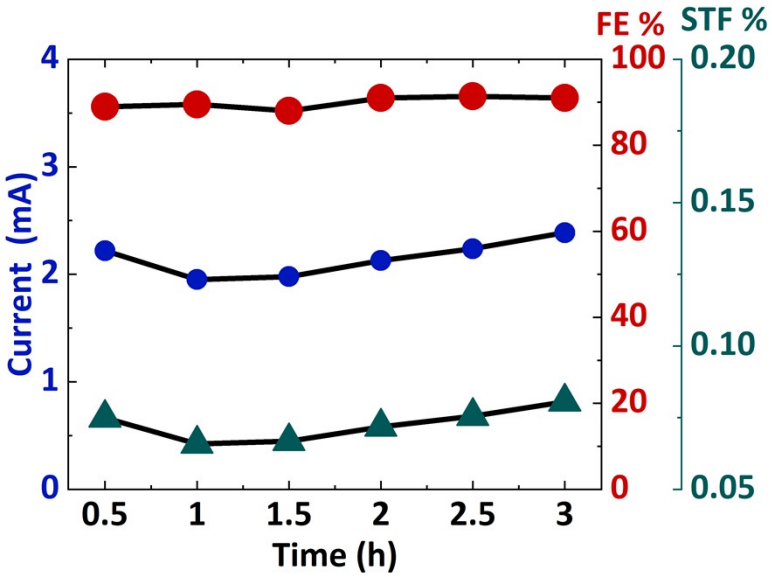

Figure S16: Stable operating current, FE of NH_3, and STF efficiency for the reduction of simulated wastewater containing just 3mM Nitrates over 3 hours.

References

(1) McEnaney, J. M.; Blair, S. J.; Nielander, A. C.; Schwalbe, J. A.; Koshy, D. M.; Cargnello, M.; Jaramillo, T. F. Electrolyte engineering for efficient electrochemical nitrate reduction to ammonia on a titanium electrode. *ACS Sustainable Chemistry & Engineering* **2020**, *8*, 2672-2681.

(2) Wang, Y.; Xu, A.; Wang, Z.; Huang, L.; Li, J.; Li, F.; Wicks, J.; Luo, M.; Nam, D.-H.; Tan, C.-S. Enhanced Nitrate-to-Ammonia Activity on Copper–Nickel Alloys via Tuning of Intermediate Adsorption. *Journal of the American Chemical Society* **2020**, *142*, 5702-5708.

(3) Wang, Y.; Zhou, W.; Jia, R.; Yu, Y.; Zhang, B. Unveiling the Activity Origin of a Copper-based Electrocatalyst for Selective Nitrate Reduction to Ammonia. *Angewandte Chemie* **2020**, *132*, 5388-5392.

(4) Chen, G.-F.; Yuan, Y.; Jiang, H.; Ren, S.-Y.; Ding, L.-X.; Ma, L.; Wu, T.; Lu, J.; Wang, H. Electrochemical reduction of nitrate to ammonia via direct eight-electron transfer using a copper–molecular solid catalyst. *Nature Energy* **2020**, *5*, 605-613.

(5) Wu, Z.-Y.; Karamad, M.; Yong, X.; Huang, Q.; Cullen, D. A.; Zhu, P.; Xia, C.; Xiao, Q.; Shakouri, M.; Chen, F.-Y. Electrochemical ammonia synthesis via nitrate reduction on Fe single atom catalyst. *Nature Communications* **2021**, *12*, 1-10.

(6) Deng, X.; Yang, Y.; Wang, L.; Fu, X. Z.; Luo, J. L. Metallic Co Nanoarray Catalyzes Selective NH3 Production from Electrochemical Nitrate Reduction at Current Densities Exceeding 2 A cm− 2. *Advanced Science* **2021**, *8*, 2004523.

(7) Wang, Z.; Young, S. D.; Goldsmith, B. R.; Singh, N. Increasing electrocatalytic nitrate reduction activity by controlling adsorption through PtRu alloying. *Journal of Catalysis* **2021**, *395*, 143-154.

(8) Liu, J.-X.; Richards, D.; Singh, N.; Goldsmith, B. R. Activity and selectivity trends in electrocatalytic nitrate reduction on transition metals. *ACS Catalysis* **2019**, *9*, 7052-7064.

(9) McCrory, C. C.; Jung, S.; Ferrer, I. M.; Chatman, S. M.; Peters, J. C.; Jaramillo, T. F. Benchmarking hydrogen evolving reaction and oxygen evolving reaction electrocatalysts for solar water splitting devices. *Journal of the American Chemical Society* **2015**, *137*, 4347-4357.

(10) McCrory, C. C.; Jung, S.; Peters, J. C.; Jaramillo, T. F. Benchmarking heterogeneous electrocatalysts for the oxygen evolution reaction. *Journal of the American Chemical Society* **2013**, *135*, 16977-16987.

(11) Morales, D. M.; Risch, M. Seven steps to reliable cyclic voltammetry measurements for the determination of double layer capacitance. *Journal of Physics: Energy* **2021**.